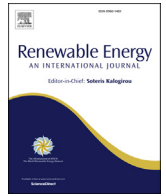




Contents lists available at ScienceDirect

Renewable Energy

journal homepage: www.elsevier.com/locate/renene

3D modelling of impacts from waves on tidal turbine wake characteristics and energy output

Sufian. F. Sufian, Ming Li*, Brian A. O'Connor

School of Engineering, University of Liverpool, Brownlow Hill, L69 3GH, UK

ARTICLE INFO

Article history:

Received 8 October 2016

Received in revised form

11 April 2017

Accepted 13 April 2017

Available online xxx

Keywords:

Virtual blade model

Horizontal axis tidal turbine

CFD

Wake characteristics

Wave

ABSTRACT

A Virtual Blade Model is coupled with a CFD model to simulate impacts from a Horizontal Axis Tidal Turbine under combined surface waves and a steady current. A two-equation model is used to represent the turbulence generation and dissipation due to turbine rotation and background wave-current flows. The model is validated against experimental measurements, showing good agreement in both surface elevation and fluid hydrodynamics. It is then scaled up to investigate a steady current with large stream-wise surface waves in the presence of a turbine. A strong interaction is found between surface wave-induced flows and that around the turbine, which clearly impacts on both hydrodynamics within the wake and wave propagation, and produces large fluctuations in power production. Model results show that the wave-period-averaged velocities are similar to those in the steady-current-only condition. However, the wave enhances the turbulence immediately behind the turbine and reduces the length of the flow transition. The wave height reduces by about 10% and the wavelength extends by 12% when propagating over the turbine region in comparison with the no-turbine condition. The wave shape also becomes asymmetric. Compared with the current-alone situation, the model results suggest that the power production is similar. However, wave oscillation produces noticeably larger fluctuations.

© 2017 The Authors. Published by Elsevier Ltd. This is an open access article under the CC BY license (<http://creativecommons.org/licenses/by/4.0/>).

1. Introduction

In recent years, the Horizontal Axis Tidal Turbine (HATT) has been regarded as one of the more promising devices for tapping tidal stream energy, which is both reliable and predictable with good potential in many sites around the world. In general, tidal turbines are placed underwater to convert the kinetic energy of tidal flow into electricity through blades rotation. Although the principle is very similar to that for wind turbines, the HATTs are designed differently due to the much larger density of seawater than that of the air [23]. More importantly, at the identified potential sites, the wind-generated surface waves are also often strong and can penetrate to considerable depth and introduce additional oscillatory effects on local flows, see Tatum et al. [21]; Bahaji et al. [2] and Veron et al. [24]. Recent research has shown that when tidal turbines operate under combined current and waves, the changes in free surface has a significant influence on wake characteristics, e.g. Bahaj et al. [2]; Consul et al. [5]; de Jesus

Henriques et al. [7]; Lust et al. [12]. Unfortunately, so far, only a handful of studies on offshore HATTs involve surface waves. The majority of them also concentrate on turbine performance under much simplified conditions at laboratory scale [21]. The effects of surface waves on the mean flow structure, turbulence, flow-structure interactions and hence the turbine power generation, and vice versa the turbine presence effects on the surface wave dynamics are not been fully understood as yet.

Alongside laboratory experiments, Computational Fluid Dynamics (CFD) modelling has been used in several studies to investigate HATTs under combined waves and current conditions. However, the challenge lies on the modelling of both free surface waves and the flow-turbine interactions. Without resolving details of free surface effects, the wave motion in previous studies has been represented in models via an added periodic oscillatory pressure at the top boundary (rigid lid) of the modelled area, e.g. Holst et al. [10]. Inevitably, the rigid lid limits the motion of fluid near the top boundary and hence the wave induced fluid flow in the vertical direction is missing in the results. This may be adequate for small waves in deep water but not for large storm waves which can affect the seabed. A more realistic approach involves the Volume of Fluid (VoF) method to track the interface between water and air, such as

* Corresponding author.

E-mail addresses: sfuads@liverpool.ac.uk (Sufian.F. Sufian), mingli@liverpool.ac.uk (M. Li), b.a.oconnor@liverpool.ac.uk (B.A. O'Connor).

earlier work of Sun et al. [20]. Similarly, two different approaches are commonly used to represent the stream turbine in a CFD model: a parameterised approach or a blade-resolving approach. The blade-resolving approach requires meshing out each blade in details and rotating multiple frames of reference to compute the flow around the blades, e.g. Mason-Jones et al. [14] and Holst et al. [10]. This type of approach requires over several millions computational nodes to cover the computational domain and each turbine blade for realistic applications, see O'Doherty et al. [18]. The parameterised approach, on the other hand, is a much simpler approach in which the effects of turbine blade rotation is represented by a static porous disk or via added sink terms in the momentum equations, such as the Virtual Blade Model (VBM) based on the Blade Element Method. The porous disk approach is much easier to implement in CFD and the computational cost is the lowest in comparison with other methods [9,20,25]. However, it is unable to resolve the details of flow structure around the turbine and is mainly used for large scale, far-field and multiple turbine simulations. In comparison, the VBM is able to replicate the rotation movement with reasonable computational cost without presenting the actual blades, but instead, simulates the motion of the fluid surrounding the blades. It can be used to simulate near-wake regions from one turbine diameter downstream and provides a useful compromise solution where reasonable accurate results can be achieved when assessing turbine performance and capturing near-wake processes [4].

It is therefore considered that the best optimal approach is obtained by combining the VoF method to resolving the surface wave dynamics alongside with the VBM method to represent the turbine: moderate computational costs than results. However, it should be noted that the VBM was originally designed for a turbine within a single phase fluid, which is strictly speaking not applicable in multi-phase calculations based on the VoF scheme. The present study will test the VBM method by ensuring that the turbine is submerged in the water without any exposure to the air so as to avoid the above complication. The combined approach will be able to provide more evidence on the wave impacts on turbine wake characteristics and power outputs as well as the impact of the turbine on the wave processes. In addition, this study will differ from earlier works [20,21], where more vigorous flow conditions (storm conditions) can be simulated and the impacts from a typical field-scale turbine are considered, thereby benefiting from the lower computational efforts.

The outline of the present paper is as follows. Section 2 presents the modelling system, while the model implementation and validation against de Jesus Henriques et al. [6] experiment are discussed in Section 3. Section 4 presents the model application to a field-scale turbine under combined waves with a steady current. Finally, a summary and conclusions are given in Section 5.

2. Numerical model

2.1. Governing equations

ANSYS FLUENT 14.5 [1] was used to resolve the flow hydrodynamics by solving the Reynolds Averaging Navier-Stokes (RANS) equations via the finite-volume method. The coordinate system is defined as x in the stream-wise, y in the vertical and z in the span-wise directions, respectively, as shown in Fig. 1. The turbine is placed at typically 1/3 of the depth from the surface. Air is assumed to occupy the space above the water.

The pressure and velocity fields are obtained from the Navier-Stokes equations averaged over a time period longer than the turbulent time scale (RANS):

$$\frac{\partial \rho}{\partial t} + \frac{\partial \rho \bar{v}_i}{\partial x_i} = 0 \quad (1)$$

$$\frac{\partial}{\partial t} (\rho \bar{v}_i) + \frac{\partial}{\partial x_i} (\rho \bar{v}_i \bar{v}_j) = -\frac{\partial p}{\partial x_i} + \frac{\partial}{\partial x_j} \left[\mu \left(\frac{\partial \bar{v}_i}{\partial x_j} + \frac{\partial \bar{v}_j}{\partial x_i} - \frac{2}{3} \delta_{ij} \frac{\partial \bar{v}_l}{\partial x_l} \right) \right] + \frac{\partial}{\partial x_j} \left(-\rho \overline{v'_i v'_j} \right) + F_i \quad (2)$$

where ρ is the density of the fluid; v_i are the instantaneous flow velocities along the x (u), y (v) and z (w) directions, respectively; p is the total pressure; F_i is the external body force in the i -th direction; and μ is dynamic viscosity. The over-bar denotes time-averaged values and the v'_i refers to the fluctuation in velocity v_i , e.g. $v_i = \bar{v}_i + v'_i$. The RANS equations can be closed using different turbulence models based on the Boussinesq hypothesis:

$$-\rho \overline{v'_i v'_j} = \mu_t \left(\frac{\partial \bar{v}_i}{\partial x_j} + \frac{\partial \bar{v}_j}{\partial x_i} \right) - \frac{2}{3} \rho k \delta_{ij} \quad (3)$$

where μ_t is the turbulence eddy viscosity, $k = \frac{1}{2} \overline{v'_i v'_i}$ is the Turbulent Kinetic Energy (T.K.E.) and δ_{ij} is the Kronecker delta. For simplicity, the over-bar is omitted in the following sections.

Following El-Beery [8]; a two-equation turbulence model, Shear Stress Transport (SST) $k - \omega$, is adopted in the present study to simulate turbulence generation and dissipation. In particular, the $k - \omega$ formulation is employed in the main free-stream fluid body and the calculation switches to a viscous sub-layer model near the wall boundary, which combines the advantages of both methods as shown in Menter [15]. The SST modifies turbulent viscosity formulation to account for the transport effects of the principal turbulent shear stress. In addition, the SST model incorporates a damped cross-diffusion derivative term in the ω equation, which makes it better for adverse pressure gradient flows. El-Beery [8] demonstrates that the SST $k - \omega$ is best by considering different turbulence generation and dissipation sources in comparison with other models. The turbulent kinetic energy, k , and special dissipation rate, ω , are computed as follows from the equations,

$$\frac{\partial}{\partial t} (\rho k) + \frac{\partial}{\partial x_i} (\rho k v_i) = \frac{\partial}{\partial x_i} \left(\Gamma_k \frac{\partial k}{\partial x_i} \right) + G_k - Y_k + S_k \quad (4)$$

$$\frac{\partial}{\partial t} (\rho \omega) + \frac{\partial}{\partial x_i} (\rho \omega v_i) = \frac{\partial}{\partial x_i} \left(\Gamma_\omega \frac{\partial \omega}{\partial x_i} \right) + G_\omega - Y_\omega + S_\omega + D_\omega \quad (5)$$

where G_k and G_ω are the generation of k and ω due to turbulent mean-velocity gradients respectively; Γ_k and Γ_ω are the effective diffusivity; Y_k and Y_ω are the dissipation due to turbulence; D_ω is the cross-diffusion term; and S_k and S_ω are user-defined source terms. The effective diffusivity Γ_k and Γ_ω are given by the equations:

$$\Gamma_k = \mu + \frac{\mu_t}{\sigma_k}; \quad G_k = -\rho \overline{v'_i v'_j} \frac{\partial v_j}{\partial x_i}; \quad Y_k = \rho \beta^* f_{\beta^*} k \omega \quad (6)$$

$$\Gamma_\omega = \mu + \frac{\mu_t}{\sigma_\omega}; \quad G_\omega = a_\omega \frac{\omega}{k} G_k; \quad Y_\omega = \rho \beta_\omega f_{\beta_\omega} \omega^2 \quad (7)$$

where σ_k and σ_ω are the turbulent Prandtl numbers for k and ω respectively, and a_ω , β^* , f_{β^*} , β_ω and f_{β_ω} are model coefficients. When SST is employed, the turbulent viscosity μ_t is defined by the equations:

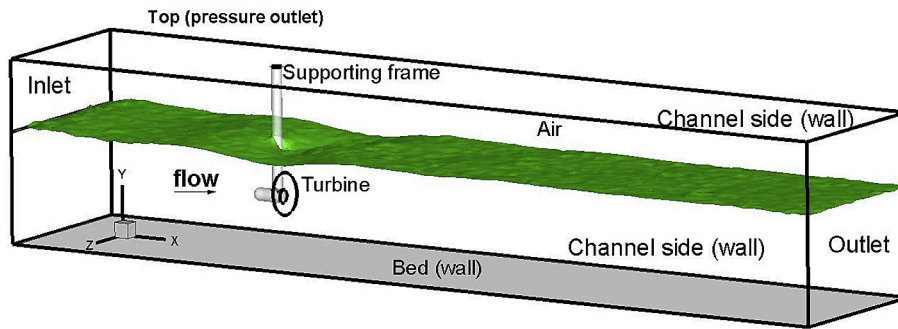


Fig. 1. Model setup.

$$\mu_t = \frac{\rho k}{\omega} \frac{1}{\max\left(\frac{1}{a^*}, \frac{SF_2}{a_1 \omega}\right)} \quad (8)$$

$$F_2 = \tanh \left[\left[\max \left(\frac{2\sqrt{k}}{0.09\omega y}, \frac{500\mu}{y^2\omega} \right) \right]^2 \right] \quad (9)$$

where S is the strain rate magnitude; F_2 is the blending function; and a^* is damping coefficient of turbulent viscosity; a_1 is the model constant (0.31). At the free surface, however, high velocity gradients are often found due to the large difference in the density between the water and air, which produces high level turbulence. A turbulence damping source term, S_ω , is therefore added to the ω Equation (5):

$$S_\omega = A_i \Delta n \beta^+ \rho_i \left(\frac{B \delta \mu_i}{\beta^+ \rho_i \Delta n^2} \right) \quad (10)$$

in which A_i is the interface area density for i th-phase; Δn is the cell height normal to interface; β^+ is a model constant (0.075); and B is a damping factor.

In the present study, the Volume of Fluid (VoF) approach is used to track the free surface variations due to wave propagation. This approach is based on the concept of air-water mixture velocity as follows:

$$v_i = \alpha v_i^w + (1 - \alpha) v_i^a \quad (11)$$

where v_i^w and v_i^a are the flow velocities for the water phase and the air phase respectively; and α is the fluid volume fraction. When $\alpha = 0$, the cell is fully occupied by air; when $\alpha = 1$, the cell is full of water and when $0 < \alpha < 1$ the cell is partly filled and encloses the interface. The calculation is initialised with given volume fraction of the fluid phase through adapting the region of water to the initial water level. A surface-tracking technique is then used to solve the water and air volume fraction in each computational cell throughout the domain.

2.2. Waves generation

In the present study, the surface waves are generated by imposing a boundary condition at the inlet to the model area. The free surface elevation and corresponding flow velocity across the water body are computed according to the appropriate wave theory depending on the wave length to water depth ratio at each time step. More details can be found in ANSYS [1].

The turbulent kinetic energy, k , at the inlet is calculated from

turbulence intensity by the following equations:

$$k = \frac{3}{2} (\bar{v} T_i)^2 \quad (12)$$

where \bar{v} is the depth-mean horizontal flow velocity and T_i is the initial turbulence intensity. The corresponding special turbulence dissipation rate, ω , is found from the turbulence length-scale, l , at the inlet:

$$\omega = k^{\frac{1}{2}} c_\mu^{-\frac{1}{4}} l^{-1} \quad (13)$$

where c_μ is the model constant (0.09). The length scale is defined as:

$$l = 0.07 L_D \quad (14)$$

where L_D is the characteristic length which is taken as the hydraulic diameter of the inlet.

One of the difficulties in modelling surface waves is the prevention of wave reflections at the outlet boundary while waves are passing through it. In the present study, a damping zone is introduced to suppress this effect via adding a damping source term in the momentum Equation (2) near the outlet boundary. The source term is computed as follows:

$$F_s = -c(0.5\rho|\bar{v}|\bar{v})f(y)f(x) \quad (15)$$

where c is the damping resistance (1/m), $f(x)$ and $f(y)$ are the damping functions in horizontal and vertical directions respectively [1].

2.3. Turbine representation

The VBM simulates the effects of the blades rotation within the fluid through a body force in the x , y and z directions, which acts inside a disk of fluid with an area equal to the swept area of the turbine blade. The value of this body force is computed based on integration of rotational force from the rotors over a swept cycle, so that the details of the flow around an individual rotor can be simplified. In this way, the power generation from a HATT can be described by considering the fluid passing through a thin disk that will convert the fluid kinetic energy into rotational motion. It is assumed that this disk contains an infinite number of rotating blades and functions as an energy extractor, causing a sharp change in pressure (hydraulic jump). Bernoulli's equation is applied over this disk with the assumption that the flow is frictionless. The axial (a) and angular (a') induction factors can be defined as:

$$a = \frac{v_1 - v_2}{v_1} \quad (16)$$

$$a' = \frac{\Omega_w}{2\Omega} \quad (17)$$

where v_1 is flow velocity upstream of turbine, v_2 is the flow velocity immediately behind the turbine, Ω is the blade rotational speed and Ω_w is the wake rotational speed. The effective approaching flow containing the axial free stream and rotational flow determine the effective angle of attack β as shown below:

$$\tan\beta = \frac{\lambda_r(1 + a')}{(1 - a)} \quad (18)$$

where λ_r is the tip speed ratio.

The blade is divided into sections at a fixed radius. The drag and torque (tangential) forces are calculated on each section of the blade as in Fig. 2 using the equations:

$$S_x = dF_x = \sigma' \pi \rho \frac{V^2(1 - a)^2}{\cos^2 \beta} (C_L \sin \beta + C_D \cos \beta) r dr \quad (19)$$

$$S_\theta = dF_\theta = \sigma' \pi \rho \frac{V^2(1 - a)^2}{\cos^2 \beta} (C_L \cos \beta - C_D \sin \beta) r^2 dr \quad (20)$$

where σ' is the local solidity; C_L and C_D are lift and drag coefficients respectively, and their values are provided as part of the blade specification; r is the directional vector along the blade. S_x and S_θ are the source terms in axial and tangential directions, respectively. These source terms are added in the RANS Equation (2) in the form F_i .

To take into account the variation in C_L and C_D across the length of a blade, from root to tip, the whole blade is divided into a number of small sections. The lift and drag forces on each section are computed from 2D aerodynamics based on the angle of attack, chord length, aerofoil type, and lift and drag coefficient for each segment. The free stream velocity at the inlet boundary is used as an initial value to calculate the local angle of attack (AOA) and

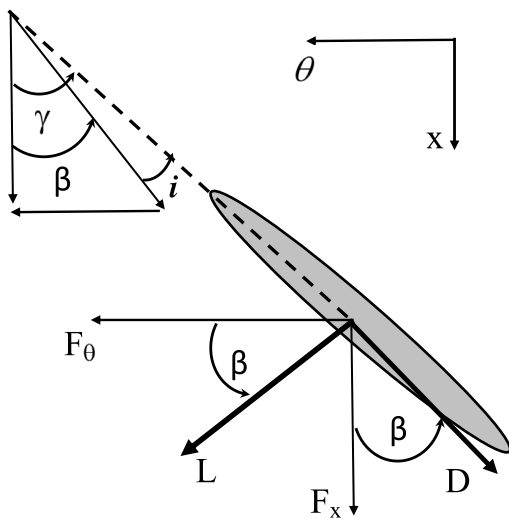


Fig. 2. Angles of lift and drag forces on blade section; β is the angle of attach; γ is the blade ration angle; L is the direction of lift force; and D is the direction of the drag force; F_x and F_θ are the force components along x and θ directions, respectively.

Reynolds number (Re) for each segment along the blade. The calculated values of AOA, lift and drag coefficients are then interpolated from a look-up table, which contains values of these variables as a function of AOA and Re [16].

In reality, however, a secondary flow at the tip of the blade will be generated when a turbine is operating, e.g. the tip vortices and radial flow [17]. This secondary flow violates the assumption of the local lift and drag forces being computed in 2D, called the rotor tip effect. To take this into account, in total 96% of the blade's span is assumed to experience lift and drag and the remaining 4% to be affected by drag force alone.

For each different tidal turbine, the corresponding tip speed ratio varies, which affects the operation of the turbine and hence the simulation as described above. In the present work, the turbine tip speed ratio is kept at 5.5, corresponding to the turbine used in the laboratory experiment model validation tests. The value can be changed when a particular turbine configuration is given, but the overall results in terms of the objectives of the present work are expected to be broadly similar.

2.4. Power measures

The power produced by the turbine is computed based on the power coefficient c_p proposed in de Jesus Henriques et al. [7] times the power available at the turbine site:

$$P = \frac{1}{2} \rho C_p \bar{v}^3 A_t \quad (21)$$

where \bar{v} in the horizontal mean velocity across the turbine surface; and A_t is the area swept by the blade.

2.5. Boundary conditions

There are five different types of boundary conditions involved in the model simulation: inlet, outlet, bed, channel top and side walls, see Fig. 1. At the inlet boundary, the velocity components, as well as the background turbulence intensity and hydraulic diameter are defined. The velocity is set to be perpendicular to the boundary with an initial gauge pressure of zero.

Under a combined waves and current condition, the flow velocity at the inlet includes both steady current and surface wave-induced oscillatory flows. The wave-induced velocity components are calculated according to the particular wave theory appropriate for the simulation as introduced previously. In the present work, linear wave theory and Stokes 2nd order wave theory were used since the wave length-water to water depth ratio was limited between the shallow water wave and deep water wave conditions. At each time step, the free surface level is specified according to the wave theory or experimental conditions, if available.

The channel sides are defined as walls with slip conditions to minimise the side-wall effects. The bed is specified as a non-slippery boundary with specified roughness height. The top of the channel has an open-air boundary condition where the pressure is set to atmospheric.

At the model outlet, the pressure is specified based on the free surface level projected from the volume fraction values at the neighbouring cell inside the computational domain. A damping zone is introduced to suppress the wave reflection via adding a damping source term in the momentum equation as shown in Equation (15).

2.6. Solution methods

The computational domain is discretised using an unstructured

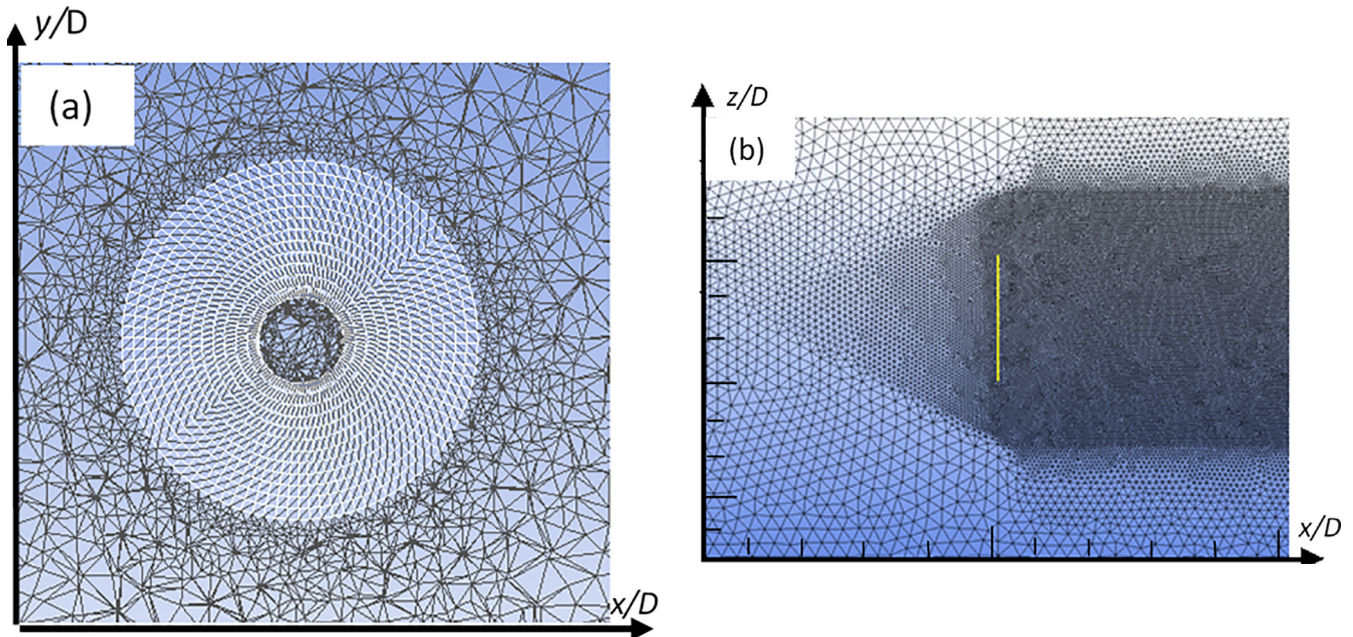


Fig. 3. Computational mesh around turbine (a) and distribution across the width of the channel (b).

hybrid mesh as shown in Fig. 3. The hexahedron cells are generated over the turbine swept area by applying a 3D blocking procedure in order to have a uniform node distribution around the disk for VBM to be able to function (Fig. 3a). The rest of the channel is discretised using tetrahedral cells with varying density across the channel: high resolution immediately in front and behind the wake area as shown in Fig. 3b.

In the present study, the Pressure-Implicit with Splitting of Operators (PISO) pressure-velocity coupling scheme is used to solve the governing differential equations [1]. An implicit scheme is used for temporal discretisation to reduce the limitation on time step size and keep the simulation stable. The Green-Gauss theorem is used for discretisation of spatial gradients of scalars at cell centres. Node-based gradient evaluation is used for the turbine region when implementing VBM to get high accuracy [1].

The momentum, volume fraction, turbulent kinetic energy and specific dissipation rate are all computed using the Quadratic Upstream Interpolation for Convective Kinematics (QUICK) scheme, which is based on an average of the weighted and centre interpolation of the variable. This scheme is selected for its higher accuracy when compared with upwind schemes [11]. At each time step, the convergence criteria are also checked so that normalised residuals for all variables are lower than 10^{-5} .

2.7. Mesh sensitivity

A number of tests were conducted to assess the model's accuracy for flow velocity based on different mesh resolution at the turbine face and in the wake region in order to identify the required mesh resolution for a mesh-independent solution. These tests were setup according to the experimental condition in Tedds et al. [22]. The dimensions of the flume in these latter experiments was 3.7 m long, 1.4 m wide with a water depth kept at 0.85 m with a 0.5 m diameter three-bladed turbine centred at mid-depth. A steady water flow with cross-section averaged speed of 0.9 m/s and 3% turbulence intensity was imposed at the inlet. Fig. 4 shows the comparison of computed stream-wise velocity (u) against the measured data across the width of the channel at 2 turbine

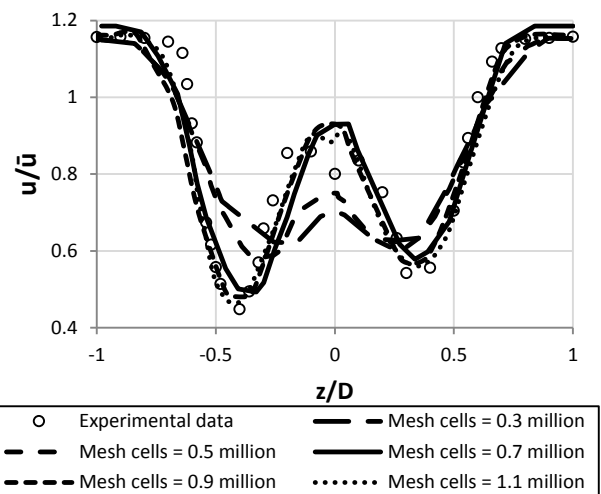


Fig. 4. Comparison of computed stream-wise velocity (u) at 2D behind the turbine for different mesh resolution. \bar{u} is the inlet flow velocity, D is the turbine diameter.

Table 1
Model CPU time and corresponding averaged error for different mesh sizes.

Tests	Total Mesh Cells (million)	CPU Time (hour)	Error (%)
1	0.3	4	40
2	0.5	6	29
3	0.7	9	11
4	0.9	14	9
5	1.1	21	8

diameters downstream. Table 1 also summaries the average errors and the corresponding CPU time for these different mesh configurations.

It is obvious that the accuracy of the model improves with increasing mesh resolution. Once the number of mesh cells are

Table 2
Wave conditions used in the model calibration.

Wave Height H(m)	Period T(s)	Wavelength L(m)	H/L	Current speed V (m/s)	Ursell number (HL^2/D^3)
0.082	0.75	2.00	0.041	0.9	0.75

beyond 0.7 million, the difference in the errors tends to be small. The required computational efforts, however, increases dramatically. It was, therefore, decided to employ 0.7 million cells to cover the turbine face, which requires at least 20 mesh nodes across the whole length of a blade.

Apart from turbine representation, the model accuracy in surface wave dynamics is also very important in the present study. To resolve the surface wave propagation, it was often critical to consider the temporal step size across a wave period, and the number of nodes over one wave length. Several tests with combined current and waves were therefore carried out to simulate wave-current interactions in a channel without turbine influences. The experiment conducted by de Jesus Henriques et al. [6] was used to validate the model's prediction. A sinusoidal linear wave was generated by a paddle wave maker in the same flume as that in Tedds et al. [22] with 0.76 m depth of water. Table 2 lists the corresponding wave characteristics. A steady cross-section averaged current of 0.9 m/s was imposed at the inlet in the same direction as the wave propagation.

Fig. 5 shows the computed surface elevation based on four different time steps over one wave period, in comparison with the measured data. Results show a remarkable improvement in the accuracy when increasing the number of time steps. When the total number of steps is more than 30, however, the model accuracy does not improve noticeably and therefore 30 steps per wave cycle was selected in the following calculations.

3. Model validation

The experiment of de Jesus Henriques et al. [6] was selected for model calibration. The experimental conditions are listed in Table 2. The model was setup using a total of approximately 1 million tetra/mixed cells. At the inlet, 2nd order Stokes wave theory was used as

suggested in de Jesus Henriques et al. [6]. The horizontal profiles of the velocity components, as well as the surface elevation at 1.5D behind the turbine, were recorded in the experiments (Fig. 6).

The model simulation continued for more than 100 wave cycles before any data was collected to ensure that the computed solution had converged. The results from the last three wave cycles were averaged to produce ensemble-averaged outputs that can be compared with the measured data.

Fig. 7 shows the computed results against the measured stream-wise velocity u in [a], vertical velocity v in [b] and span-wise velocity w in [c] at 2D, 3D and 4D downstream of the turbine positions at the level of the turbine central axis above the bed and across the width of the channel: all velocities normalised by the inlet velocity \bar{u} . The symbols are measured data and solid lines are computed results. The overall agreements are reasonable, with accuracy varying between 85% and 90% of the measured values on average. It is clear that the VBM is able to capture the main feature of the flow behind the turbine from $x = 2D$ and onwards, especially in the stream-wise direction which is a magnitude larger than that in vertical and span-wise directions. Certain differences in the computed and measured values can be found in the velocity along the vertical direction in [b] at $x = 3D$ and 4D where the minimum flow velocity is found at different positions in the z direction. Similarly, in [c] at $x = 2D$, the 2nd peak of span-wise velocity is not seen in the model results. These discrepancies are largely due to the fact that the VBM is based on a cycle-averaged force and therefore the blade rotation effects in both vertical and span-wise directions are not represented in great detail. It can be noted in these comparisons that the accuracy of the computed results improves noticeably when moving downstream away from the turbine.

It is also noted that in the comparison of stream-wise velocity in [a], the measured data and computed results show a similar "W" shaped distribution immediately behind the turbine and a "U"

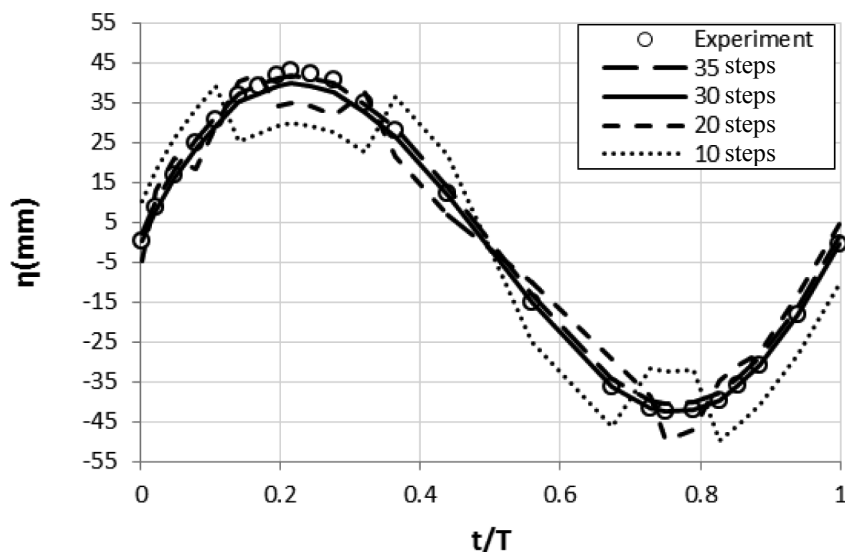


Fig. 5. Comparison of computed water surface elevation against experimental data across a wave period with 4 different time steps.

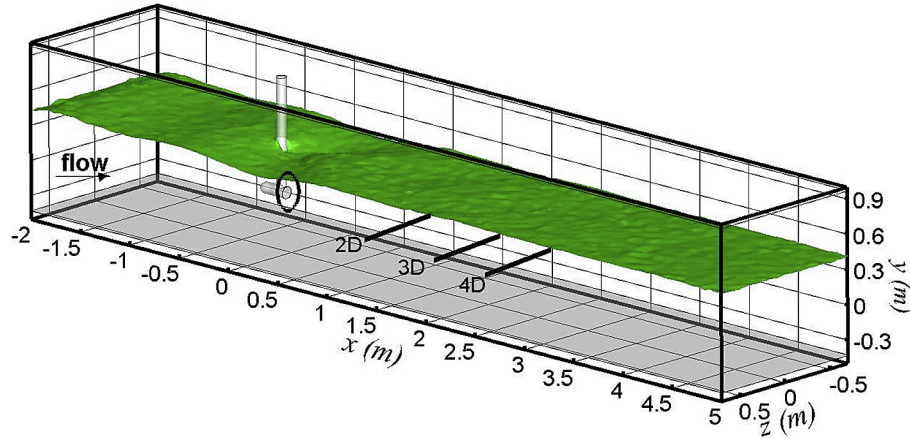


Fig. 6. Plan view of the horizontal measuring locations at 2D, 3D and 4D downstream along the channel centreline.

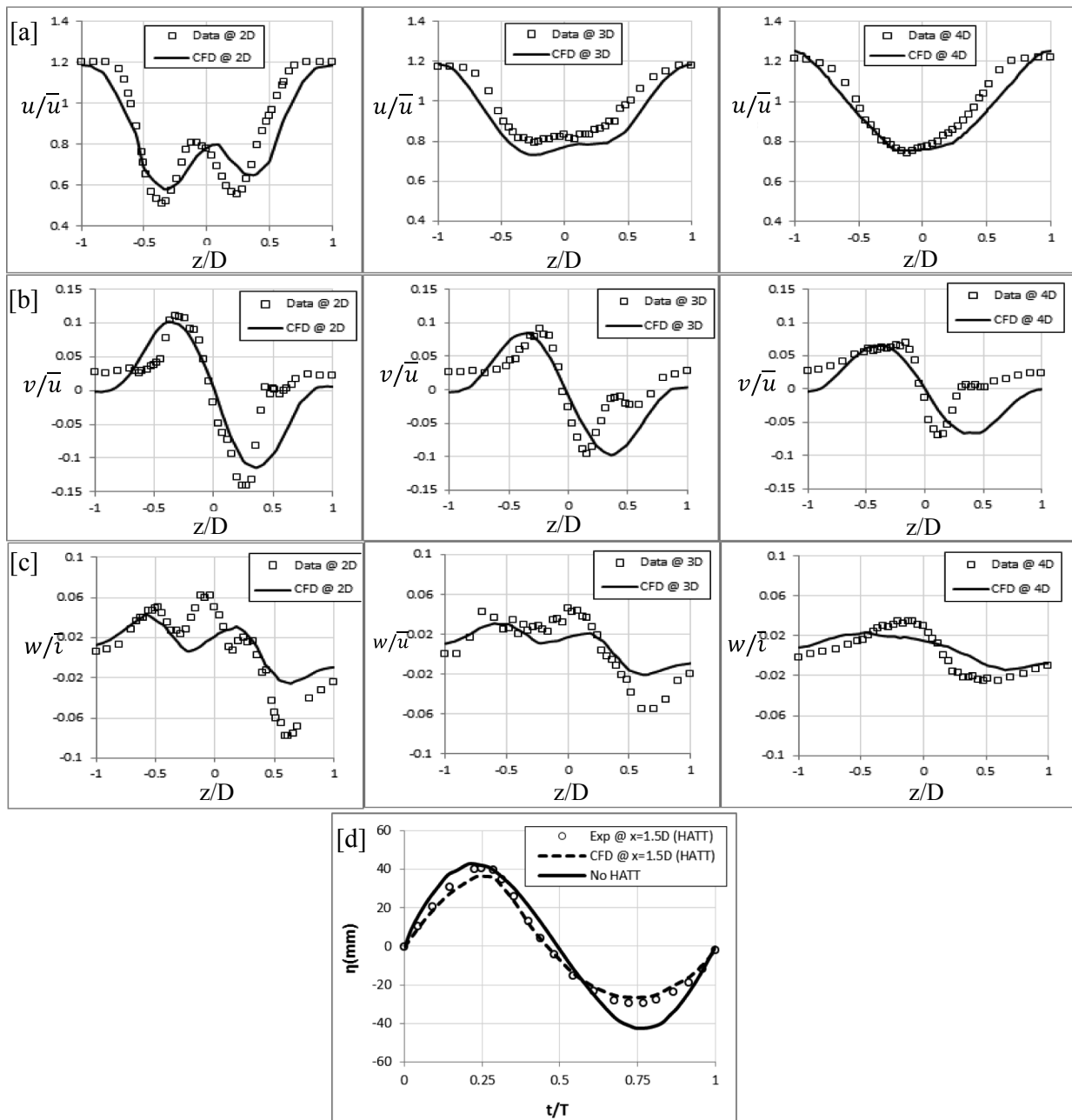


Fig. 7. Comparison of measured and computed horizontal profiles of normalised velocities u/\bar{u} in [a], v/\bar{u} in [b] and w/\bar{u} in [c] at $x = 2D, 3D, 4D$ downstream along the centreline, respectively. \bar{u} is the inflow velocity. [d] Shows a comparison of measured and computed surface elevation η with respect of time at $x = 1.5D$ downstream.

Table 3
Wave parameters.

Wave Height H (m)	Period T(s)	Wavelength L(m)	H/L	Current speed V (m/s)	Ursell number (HL^2/D^3)
5.34	14.8	293	0.0167	2.00	2.12

shape from 4D further downstream. This feature is also seen in the steady-flow-only condition [19]. However, it is found that when waves are present, the changes in velocity distribution from a “W” shape to a “U” shape take place at $x = 4D$, whereas in the steady-current-only condition, the changes are delayed until $x = 6D$ as shown in Sufian and Li [19]. The difference indicates that the presence of waves enhances fluid mixing and therefore reduces the length of flow transition from a highly separated flow to a well-mixed one.

The computed surface elevation at $x = 1.5D$ downstream of the turbine is compared with the measured values over one wave cycle in [d]. As a comparison, the result without a turbine is also shown in the figure denoted by a solid line. The computed results and the experimental data show that the wave shape clearly differs from that when the turbine is absent. The wave height reduces by almost 17%, largely due to the reduction in water level during the wave trough (offshore) period. In addition, a slight wave phase shift becomes clear and the wave shape deviates from its original form as it becomes non-linear and closer to a Stokes 3rd order wave.

4. Model application

After the model had been validated, it was scaled up to simulate a field-scale operation for conditions similar to that suggested by Black and Veatch [3]. The model domain retained the same as that in the validation case and the boundary conditions were kept the same. The channel was scaled up to 100 m wide and 300 m long, and featured a free surface. The water depth was 60 m with a steady flow of 2 m/s, giving a Re of 2.18×10^8 . The turbine diameter was 15 m, positioned at $2/3rd$ of the depth from the mean water level (MWL) at 100 m away from the inlet to avoid any boundary effects. The turbine operated at a tip speed ratio of 5.5 at all times, producing a blockage ratio effect of 2.9%. The model discretisation followed the same mesh generation techniques as that of experimental case to avoid inconsistency and used a total of 1.4 million tetra/mixed cells.

The defined wave at the inlet was 5.34 m in height, the wavelength 293 m and wave period 14.8s (Table 3). Linear wave theory was used to generate the boundary values at the inlet for this case. These parameters are typically found in UK waters during storms [3]. The background turbulence intensity was kept low to avoid its interference with the wave-current generated turbulence. To illustrate the results clearly, the whole water column is divided into three regions in the vertical direction where the velocity profiles show very different behaviours i.e., the upper surface layer $y/D > 2.5$, turbine-affected layer $0.5 < y/D < 2.5$ and bed boundary layer $y/D < 0.5$ as shown in Fig. 8.

The calculations were initialised using the steady-flow velocity at the inlet with a flat water surface and then integrated forward for more than 100 wave cycles before the results were collected at interval of 1 s. However, due to space limitation, the analysis is based on results at 0° , 90° , 135° , 225° and 270° as shown in Fig. 9 only.

To assist the analysis, wave-period-averaging was conducted based on the following method,

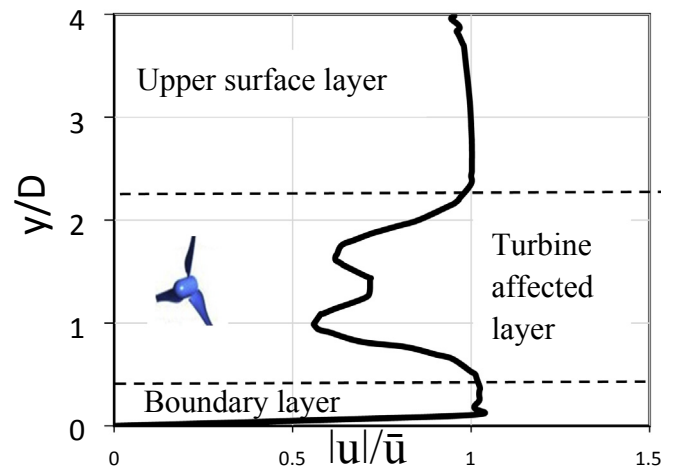


Fig. 8. Distribution of the three layers in the water column; u is the stream-wise flow velocity; \bar{u} is the inflow velocity; D is the turbine diameter.

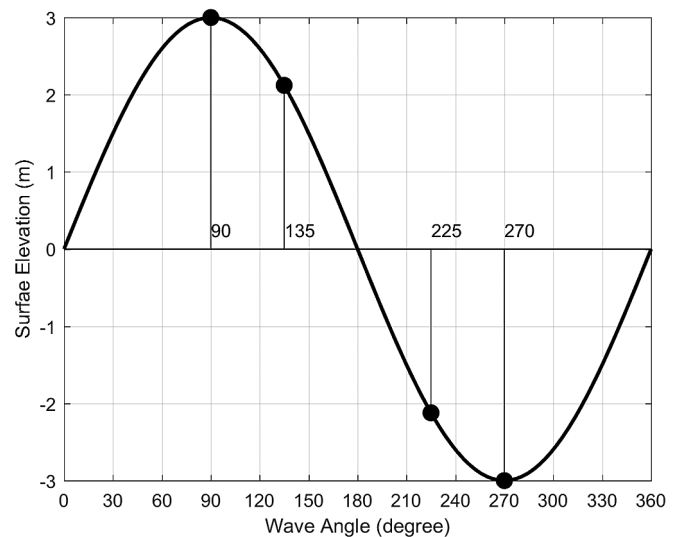


Fig. 9. The selected 4 wave phases at which the results are compared with measurements.

$$\langle \phi \rangle = \frac{1}{T} \int_0^T \phi dt \quad (22)$$

in which T is wave period, ϕ is the instantaneous variable, $\langle \phi \rangle$ is the wave-period-averaged value.

Fig. 10 presents the vertical profiles of stream-wise velocity at 1D, 2D, 3D and 4D downstream along the centre plane (across the width) of the channel at the five selected wave phases. It is found that the maximum velocity is under the wave crest (90°) and the

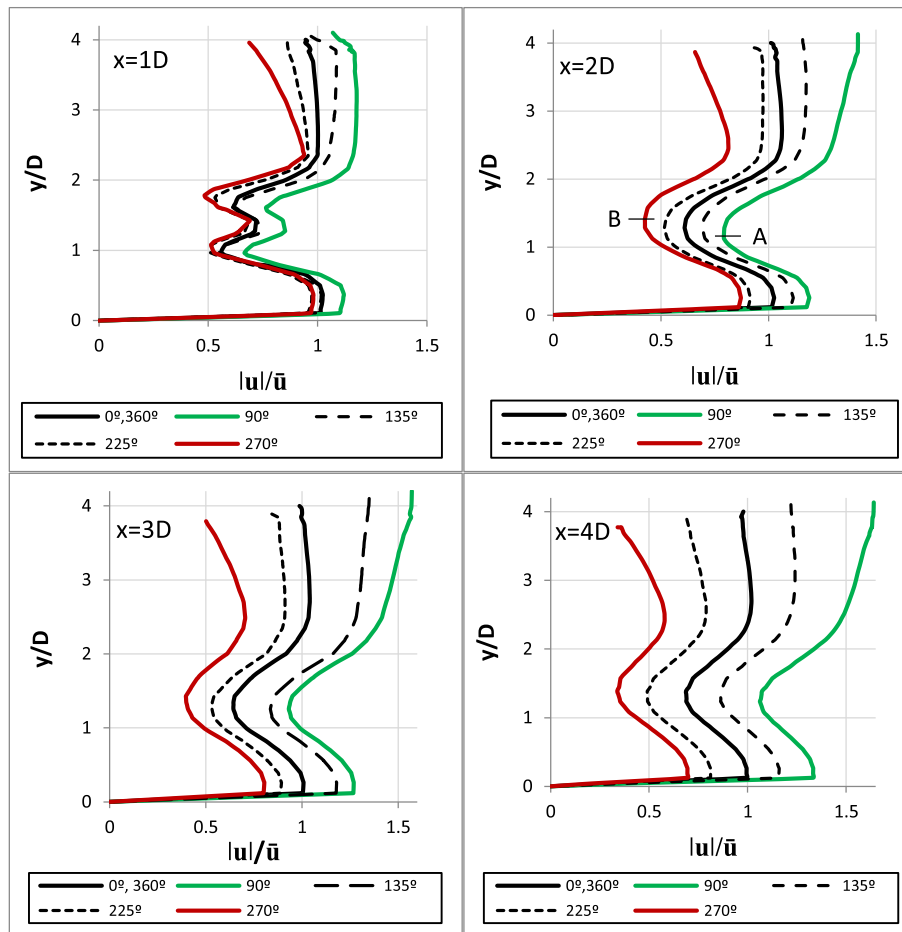


Fig. 10. Vertical profiles of stream-wise velocity at 1D, 2D, 3D and 4D downstream (centreline) at wave angle of 0° , 90° , 135° , 270° and 360° ; $|u|$ is stream-wise flow velocity; \bar{u} is the inflow velocity; D is turbine diameter.

minimum velocity is under wave trough (270°). It is also noticed that the differences in velocity over one wave cycle are larger close to the free surface in the upper surface layer than that down below, which is consistent with the fact the wave-induced orbital motion decays over the depth. In contrast, the wave effects on near-bed boundary layer processes are not obvious, although different boundary layer thicknesses can be seen in these figures.

The above figures show that the vertical position of the maximum velocity reduction varies at different phases of the wave. For example, at $x = 2D$, under the wave crest (90°), the elevation of velocity minimum is slightly below $y/D = 1.3$, as marked with A, while under wave trough (270°), the position of the velocity minimum is slightly above $y/D = 1.3$, as marked with B. This is due to the flow speed reaching its maximum strength at 90° with a higher water head. As a result, the wake moves downwards towards the bed. Under the wave trough (270°), the opposite takes place where the pressure above the turbine reduces causing the wake downstream of the turbine to rise up. This indicates that the wake is constantly lifted and suppressed throughout the wave cycle. However, the turbine-affected region more or less remains the same part of the water column, e.g., $0.5 < y/D < 2.5$ at all the positions considered.

It is also noted that the variation in flow speed between wave crest (90°) and wave trough (270°) becomes larger moving further downstream. For example, at $x = 2D$, the difference between maximum and minimum velocities is above 75% of the inflow velocity and such variation increases at 3D to 100% and 4D to 130%.

This is due to the fact that close to the turbine, the current undergoes strong transition and the wave oscillatory effect is comparatively less significant. Moving away from the turbine, wake recovery takes place and the wave is able to penetrate through to cause noticeable variation in velocity at different phases. It is therefore clear that turbines suppress the wave motion by minimising the velocity variation within a distance of 4D downstream.

Fig. 11 compares vertical profiles of wave-period-averaged stream-wise velocity magnitude at 1D, 2D, 3D and 4D downstream for with and without the turbine present. It is clear that the wave-period-averaged flow velocity largely follows a similar distribution as that in steady current cases [19], e.g., accelerated flow above and below the turbine and strong velocity reduction at turbine affected region. It is also noticed that the “W” shape in velocity profile changes to a “U” shape after 2D behind the turbine, unlike the validation case (3D). This is partly due to the difference in blockage ratio between the two cases, wherein the validation test it is 16.5% but in this case, it is only 2.9%. At higher blockage, the turbine experiences a stronger pressure change at the turbine face, which consequently causes the flow to accelerate faster around the turbine and the hub-blade gap, but higher flow deficits behind the blades. In addition, the surface waves in the laboratory validation case are also much weaker than those in the present field case, which leads to less noticeable effects than the present field case.

Fig. 12 compares the vertical profiles of stream-wise velocity under a steady current alone and that under combined waves with a current after wave-period-averaging at $x = 1D$ and $x = 4D$.

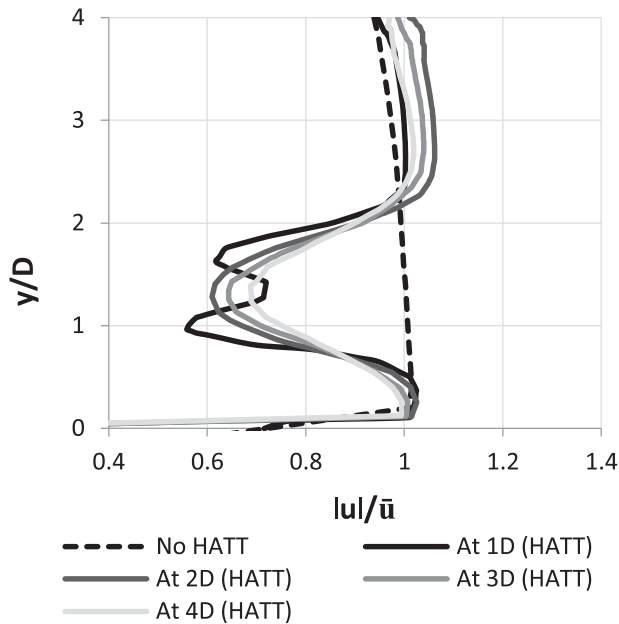


Fig. 11. Vertical profiles of wave-period-averaged velocity magnitude at 1D, 2D, 3D and 4D downstream (centreline) when stream-wise waves are present. It also shows the mean inlet velocity profile.

Overall, the two cases show similar flow behaviours. At both positions, however, the speed reduction in the combined flow tends to be less than that in the steady flow case as discussed above in the turbine affected region. At 4D position, the larger wave-induced boundary layer flow in the near bed region is apparent in comparison with the steady flow condition, together with stronger flow reduction near the surface.

Fig. 13 shows a snapshot of velocity over the flow depth through the turbine centre when the wave crest is above the turbine (90°) for no turbine in [a], with turbine in [b], and across the channel at the turbine level in [c]. It is clear in [a] that the waves have a significant impact on the flow pattern across the depth. When the turbine is in place as in [b], the wake behind the turbine is clearly visible, extending to the end of the channel and interacting with the wave-induced flows. The turbine-induced accelerated flow

interferes with the wave-induced flow acceleration above, as well as beneath the turbine. But further downstream, the velocity reduction is also clearly visible ($x/D = 0-3$). In the region $x = 4D - 8D$, the wave-induced flow reduction is enhanced by the turbine wake and the reduction region extends from $3D$ to $9D$. Similar behaviours are seen in the horizontal plane [c] where the turbine interferes with the wave-induced oscillatory flows.

In Fig. 13 [b], a new low velocity region in $3D < x < 10D$ in horizontal and $0.5D < y < 2D$ in the vertical is clearly visible underneath the wave trough, which also extends to the region under the following wave crest in $9D < x < 13D$. This is due to the interaction between the turbine wake and wave-induced oscillations in the water. When such reduction is superimposed on the wave oscillating flow, the lower flow speed under the wave trough is further reduced.

Fig. 14 shows a snapshot of velocity distribution when the wave trough is above the turbine (270°) across the flow depth for no turbine in [a], with the turbine in [b] and top-down view of the horizontal plane at turbine level in [c]. At the turbine position, the flow speed is increased above and beneath the turbine, which interacts with the wave-induced speed reduction under the wave trough. Behind the turbine, the wave-induced lower velocity region extends to $x = 5D$ (B and B'). The flow speed in the region $5D < x < 10D$ is also reduced and leads to a 50% reduction in the original flow velocity, see C and C'.

Fig. 15 presents the computed T.K.E. distribution when the wave crest is above turbine in [a] for the water depth and top-down view in [b], and when wave trough is at the turbine location for the water depth in [c] and top-down view in [d]. It is clear that wave oscillatory motion leads to strong T.K.E. generation along the water surface as the wave propagates to the turbine at $x = -2D$ as shown in both [a] and [c]. Meanwhile, the turbine rotation-generated turbulence also propagates downstream which is more or less limited within the mid layer of the water. Comparing with that under the wave trough, the overall T.K.E. level is found to be stronger during wave crest passes through in [a] and [b], approximately twice as much as that in [c] and [d]. It is also seen from the top-down view at the turbine level that higher levels of T.K.E. are found on the right side of the hub comparing to that on the left hand side. The eddy shedding behind the turbine rotor is clearly visible in the wake, especially close to the turbine.

Among these figures, there are noticeable interactions between the turbine-induced turbulence and that due to the surface waves

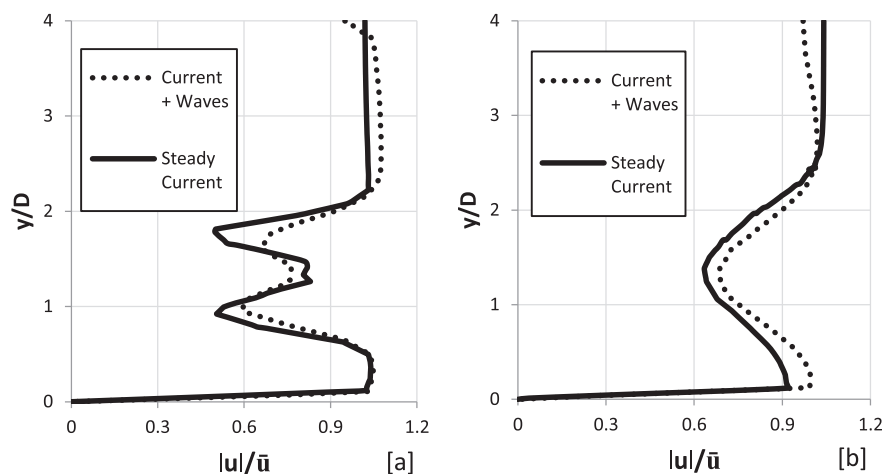


Fig. 12. Comparison between vertical profiles of wave-period averaged velocity magnitude of current + wave and steady current at [a] 1D and [b] 4D (centreline).

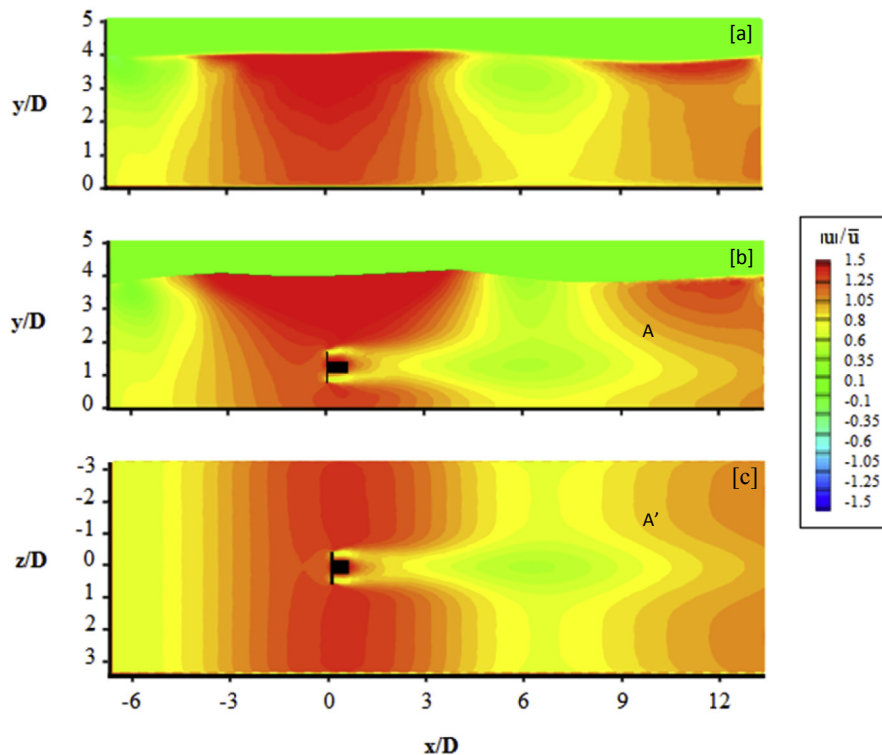


Fig. 13. Contours of stream-wise velocity over the water depth at the turbine centre when the wave crest (90°) at turbine location, [a] no turbine, [b] with turbine and [c] top-down view with turbine.

at $y = 2.5D$, starting from $x = 1D$. These interactions become stronger further downstream, as shown in Fig. 15. However, the wave-induced turbulence is generally lower than that in the turbine wake region and hence we see the turbine wake still dominates the turbulence characteristic in the water column in this particular case.

Fig. 16 shows the computed surface elevation along the channel length when the wave trough (a) and wave crest is at the turbine position (b). The black line denotes the surface elevation without turbine; the red line denotes the surface elevation when the turbine is installed.

It is found that the wave shape deforms when the turbine is installed in the channel. Such impact is expected, as Sun et al. [20] have previously observed in steady flows that the free surface experiences a slight rise in front of a turbine followed by an immediate drop. In the present study, the wave surface in front of the turbine is interrupted from descending in (a) by the turbine-induced flow acceleration near the surface. This velocity increase delays the surface drop (trough) at the turbine location to show a surface rise between $-1D < x < 2D$. Apart from the water level rise around $x = 0D$, it is also clear that there is a water level drop further downstream at approximately $x = 3D$ which subsequently rises quickly, peaking at approximately $x = 10D$. In Fig. 16(b), the flow slows down in front of the turbine and leads to a surface rise between $-2D < x < -1D$. The accelerated flow above the turbine increases the flow speed causing a surface drop that interferes with the ascending motion of the wave at $x = 0$. Further downstream, the accelerated flow dissipates and the wave crest peaks at $2D$ away from its original position. As a result of these interactions, the overall wavelength is extended by 12% of the original wavelength in these two figures. Meanwhile, the wave height is reduced by almost 13% due to the surface uplift above the turbine area.

Fig. 17 presents a top-down view of the computed free surface elevation based on the volume fraction values in (a) and corresponding stream-wise velocity magnitude in (b) at the surface layer. The volume fraction of 0.5 is used to denote the free surface level in (a). Due to the changes in flow velocity around the turbine, the wave trough area is clearly extended immediately behind the turbine position in (a). In addition, the wave diffraction behind the turbine is also noticeable as shown in the bending of the wave crest lines. The velocity magnitude in (b) at the surface undergoes rapid change, i.e., the immediate rise in the velocity behind the turbine, particularly at the centre of the channel between 0 and $1D$. Further downstream, the interaction with wave-induced oscillatory flows leads to high speed flow along the two sideways of the channel walls with reduce flow speed in the centre of the channel.

The above turbine-wave interactions are clearly the results of the presence of the turbine and its operation within the fluid. The turbine blockage effect introduces a strong change in the pressure around the turbine, which suppresses the wave introduced oscillations, especially close to the bed surface where the wave orbital motion is weak. In addition, the rotating blade creates considerable swirling motion immediately downstream of the turbine and interferes with the wave-induced flow field. However, further downstream of the turbine, the pressure drop due to the presence of the turbine becomes less significant in comparison with that due to wave oscillation. The wave orbital motion therefore is able to penetrate through the wake of the turbine and shorten the distance required for the velocity profile recovery.

Fig. 18 presents the computed power generation throughout one wave cycle, in comparison with that under only a steady current. The calculation is based on the mean velocity over the volume that covers from $-0.5D$ to $1D$ around the turbine swept area. The power coefficient C_p in Equation (21) follows that in de Jesus Henriques

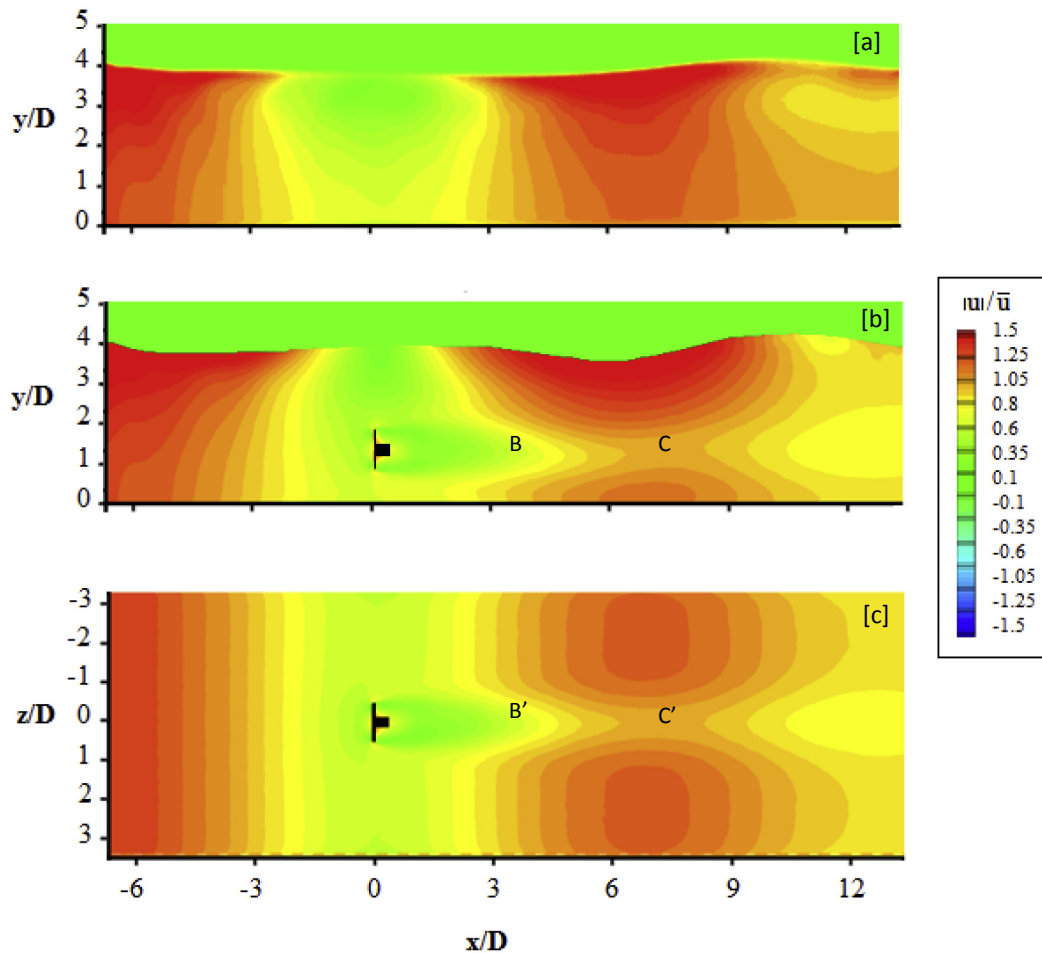


Fig. 14. Contours of stream-wise velocity across the water depth at the turbine centre when the wave trough (270°) is at the turbine location in [a] no turbine, [b] with turbine and [c] top-down view with turbine.

et al. [7]. Under a steady current, due to the eddy shedding behind the turbine, the power output over the same period of time is not constant as seen in Fig. 18. However, the magnitude of the fluctuation is considered to be small. Under the combined wave and current condition, the maximum power outputs are produced when the wave crest passes ($t/T = 0.25$), and the minimum power output occurs after the wave reverses direction ($t/T = 0.55$). On average, it can be seen that the power output is very similar to that under a steady current, which is in line with several previous studies, e.g. de Jesus Henriques et al. [7]; Tatum et al. [21]; Luznik et al. [13]. However, the fluctuations in the power output within a wave cycle are noticeable: the largest power output is almost 5–6 times the minimum values. It should be noted that the present study is based on a fixed pitch angle and a particular tip speed ratio. In field applications, either or both will be altered to optimise the turbine performance under such complex flows. In addition, the present work does not consider the flow-structure interactions in detail. As demonstrated by Tatum et al. [21]; the flow-structure interaction can have significant influences on the results. Nevertheless, the present results clearly show the potential impacts from large stormy waves on power generation from a HATTs due to the complex wave-current-turbine interactions.

5. Conclusions

In the present study, a CFD model based on an ANSYS FLUENT

model system is developed to simulate a tidal stream turbine under combined surface waves and a steady current. The turbine operation was represented by a Virtual Blade Model with the focus on the temporally-averaged flow field, rather than the instantaneous flow characteristics at individual blades. The surface waves were simulated by a VoF approach with satisfactory agreement found with the available measurements from laboratory scale studies. The model system was applied to a realistic field scale test under combined waves and current conditions to investigate potential impacts from waves on the hydrodynamics and turbulence around the turbine as well as the turbine effects on wave propagation.

The model results show that when turbines are employed in flows with propagating waves, the wave-period-averaged velocity distributions are similar to those found in steady flow conditions. It is also found that under large waves, the wake behind the turbine will change its distribution in the water body under different pressures when the wave crest and trough are passing through. The velocity-deficit-peak drops slightly in elevation when the wave crest passes and slightly rises when the wave trough is in the near-wake region. It is found that the surface waves enhance the fluid mixing behind the turbine and the local turbulence levels. Consequently, the length of the flow transition behind the turbine is shortened in comparison with the steady current condition. Further downstream, the wave is able to penetrate through the wake region and influence the recovery process. On the other hand, the surface wave-induced oscillations in velocities are also suppressed by the

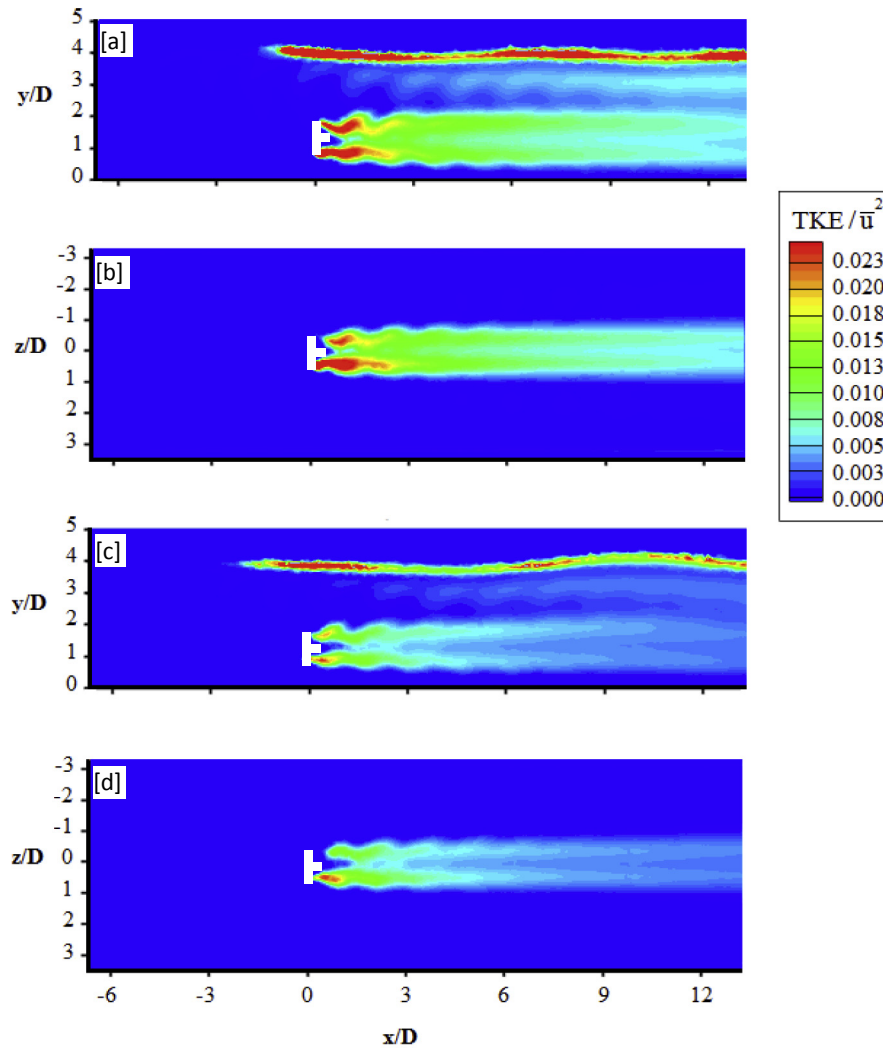


Fig. 15. Contours of TKE across the water depth and span-wise at turbine centre when the wave crest (90°) and trough (270°) are at the turbine location [a]: 90° , [b] top-down view: 90° , [c] water depth: 270° and [d] top-down view: 270° .

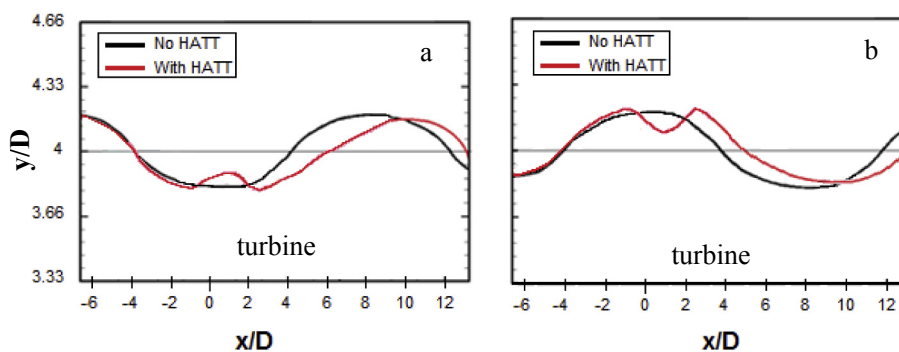


Fig. 16. Comparison of surface elevation along the channel length between with turbine and no-turbine conditions. The wave trough is above the turbine in (a) and crest is above the turbine in (b).

turbine operation around the turbine and in the near wake region.

Results from the present model also show that the turbine has an impact on wave shape. For stream-wise waves, the wavelength was found to be slightly extended by about 12% and the wave height reduced by about 10% on average. The wave shape became

highly non-linear with a steep peak at the crest and a flatter trough. Wave diffraction around the turbine site was clearly visible in the results. Comparing wave-current case with currently only case, the presence of waves was found to encourage stronger turbulence generation in the flow regime. Under large waves and a strong

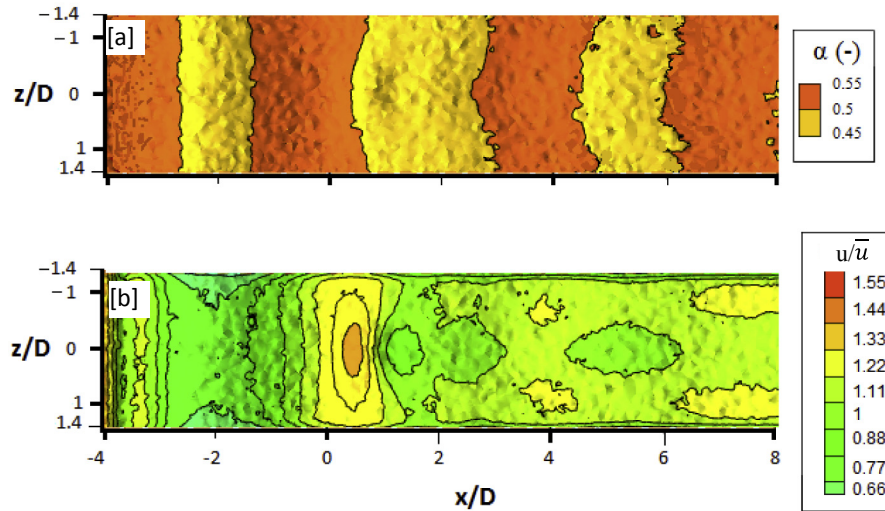


Fig. 17. Top-down view of the computed free surface elevation in (a) and corresponding stream-wise velocity magnitude in (b).

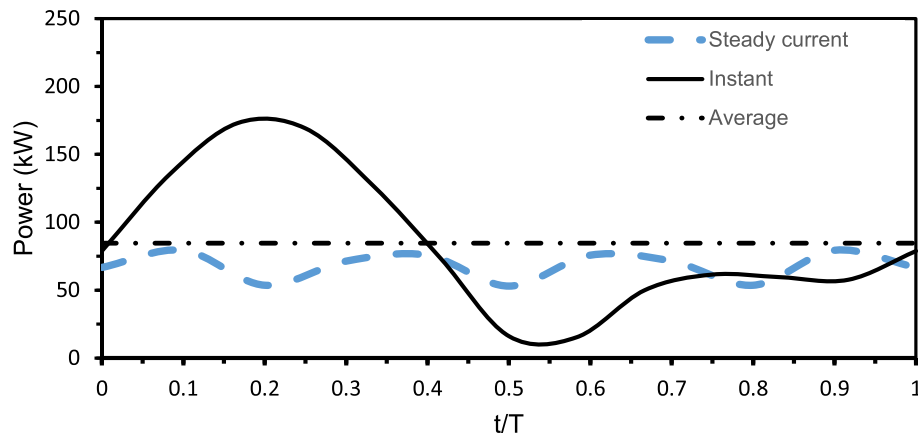


Fig. 18. Comparison of power output between waves with current and current-alone condition.

current, the turbine-induced T.K.E. extends to the upper surface layer and interacts with the upper layer under the free surface.

The predicted power generation under combined flows was found to be similar to that under a steady current. However, the wave has a strong signature in the power output within the wave cycle and leads to large fluctuations that need to be dealt with in practical applications.

Acknowledgement

The present study is partially funded by EPSRC project INSTRON (EP/J010359/1). The authors are also grateful for the general support from School of Engineering, the University of Liverpool for the first author's PhD project. Professor R. Pool and Dr Tiago A. de Jesus Henriques from the School of Engineering are thanked for providing the model calibration data.

References

- [1] I. ANSYS, ANSYS Fluent Theory Guide, 2010. USA: Issue: 13.
- [2] A.S. Bahaj, L.E. Meyers, M.D. Thomsan, N. Jorge, Characterising the wake of horizontal axis marine current turbines, in: Proceedings of the 7th European Wave and Tidal Energy Conference, University of Southampton, Porto, Portugal, 2007.
- [3] Black and Veatch, Phase 2 UK Tidal Stream Energy Assessment, The Carbon Trust, 2005. <http://www.lunarenergy.co.uk/Userimages/PhaseII/TidalStreamResourceReport.pdf> [Accessed 21 June 2014].
- [4] H. Buckland, I. Masters, J. Orme, T. Baker, Cavitation inception and simulation in blade element momentum theory for modelling tidal stream turbines, Proc. Inst. Mech. Eng. Part A J. Power Energy 227 (4) (2013) 479–485.
- [5] C.A. Consul, R.H.J. Willden, S.C. McIntosh, An investigation of the influence of free surface effects on the hydrodynamic performance of marine cross-flow turbines, in: Proceeding of Euro Wave Tidal Energy Conference, University of Southampton, 2011.
- [6] T.A. de Jesus Henriques, T. Hedges, I. Owen, R. Pool, The influence of blade pitch angle on the performance of a model horizontal axis tidal stream turbine operating under wave-current interaction, Energy 102 (2016) 166–175.
- [7] T.A. de Jesus Henriques, S.C. Tedds, A. Botsari, G. Najafian, T.S. Hedges, C.J. Sutcliffe, I. Owen, R.J. Poole, The effects of wave-current interaction on the performance of a model horizontal axis tidal turbine, Int. J. Mar. Energy 8 (2014) 17–35.
- [8] S.M. El-Behery, M.H. Hamed, A comparative study of turbulence models performance for separating flow in a planar asymmetric diffuser, Int. J. Mech. Aerosp. Ind. Mechatron. Manuf. Eng. 3 (5) (2009).
- [9] S. Gant, T. Stallard, Modelling a tidal turbine in unsteady flow, in: Proceedings of the Eighteenth International Offshore and Polar Engineering Conference, Canada, 2008, pp. 473–476.
- [10] M. Holst, O. Dahlhaug, C. Faudot, CFD analysis of wave-induced loads on tidal turbine blades, IEEE J. Ocean Eng. 40 (3) (2015) 506–521.
- [11] B.P. Leonard, A stable and accurate convective modelling procedure based on quadratic upstream interpolation, Comput. Methods Appl. Mech. Eng. 19 (1) (1979) 59–98.
- [12] E.E. Lust, L. Luznik, K.A. Flack, J.M. Walker, M.C. Van Benthem, The influence of surface gravity waves on marine current turbine performance, Int. J. Mar.

- Energy 3 (4) (2013) 27–40.
- [13] L. Luznik, K.A. Flack, E.E. Lust, K. Taylor, The effect of surface waves on the performance characteristics of a model tidal turbine, *Renew. Energy* 58 (2013) 108–114.
- [14] A. Mason-Jones, D.M. O'Doherty, C.E. Morris, T. O'Doherty, Influence of a velocity profile & support structure on tidal stream turbine performance, *Renew. Energy* 52 (2013) 23–30.
- [15] F.R. Menter, Zonal two equation $k-\omega$ turbulence models for aerodynamic flows, *Turbul. Heat Mass Transf.* 4 (1993). AIAA 93-2906. Germany.
- [16] A.T.J. Mozafari, Numerical Modelling of Tidal Turbines: Methodology Development and Potential Physical Environmental Effects, MSc. Thesis, University of Washington, 2010.
- [17] Y.C. Nho, J.S. Park, Y.J. Lee, J.S. Kwak, Effects of turbine blade tip shape on total pressure loss and secondary flow of a linear turbine cascade, *Int. J. Heat Fluid Flow* 33 (1) (2012) 92–100.
- [18] T. O'Doherty, A. Jones, D.M. O'Doherty, C.B. Byrne, Experimental and computational analysis of a model horizontal Axis tidal turbine, in: Proceedings of the 8th European Wave and Tidal Energy Conference, University of Southampton, Uppsala, Sweden, 2009.
- [19] S.F. Sufian, M. Li, 3D-CFD Numerical modelling of impacts from horizontal axis tidal turbines in the near region, in: International Conference on Coastal Engineering, World Scientific, 2014.
- [20] X. Sun, J.P. Chick, I.G. Bryden, Laboratory-scale simulation of energy extraction from tidal currents, *Renew. Energy* 33 (6) (2008) 1267–1274.
- [21] S.C. Tatum, C.H. Frost, M. Allmark, D.M. O'Doherty, A. Mason-Jones, P.W. Prickett, R.I. Grosvenor, C.B. Byrne, T. O'Doherty, Wave–current interaction effects on tidal stream turbine performance and loading characteristics, *Int. J. Mar. Energy* 14 (2016) 161–179.
- [22] S.C. Tedds, R.J. Poole, I. Owen, Experimental investigation of horizontal axis tidal stream turbine, in: Proceedings of the 9th European Wave and Tidal Energy Conference, University of Southampton, Southampton, UK, 2011.
- [23] J. Thake, Development, Installation and Testing of Large Scale Tidal Current Turbine, UK: DTI Technology Programme: New and Renewable Energy, 2005, p. 74. Report, URN Number: 05/1698.
- [24] F. Veron, W.K. Melville, L. Lenain, Measurements of ocean surface turbulence and wave–turbulence interactions, *J. Phys. Oceanogr.* 39 (2009) 2310–2323.
- [25] A.J. Williams, T.N. Croft, I. Masters, M.R. Willis, M. Cross, Combined BEM-CFD modelling of tidal stream turbines using site data, in: International Conference on Renewable Energies and Power Quality (ICREPQ'10) Journal, Granada (Spain), 2010, pp. 1560–1565. ISBN-13: 978-84-613-7543-1.